Compensation of optical heterogeneity-induced artifacts in fluorescence molecular tomography: theory and *in vivo* validation

Pouyan Mohajerani
Georgia Institute of Technology
Department of Electrical and Computer Engineering
777 Atlantic Drive North West
Atlanta, Georgia 30332
E-mail: pouyan@gatech.edu

Ali Adibi
Georgia Institute of Technology
Department of Electrical and Computer Engineering
777 Atlantic Drive North West
Atlanta, Georgia 30332

Joshua Kempner
Wael Yared
VisEn Medical, Inc.
45 Wiggins Road
Bedford, Massachusetts 01730

Abstract. We present a method for reduction of image artifacts induced by the optical heterogeneities of tissue in fluorescence molecular tomography (FMT) through identification and compensation of image regions that evidence propagation of emission light through thin or low-absorption tunnels in tissue. The light tunneled as such contributes to the emission image as spurious components that might substantially overwhelm the desirable fluorescence emanating from the targeted lesions. The proposed method makes use of the strong spatial correlation between the emission and excitation images to estimate the tunneled components and yield a residual image that mainly consists of the signal due to the desirable fluorescence. This residual image is further refined using a coincidence mask constructed for each excitation–emission image pair. The coincidence mask is essentially a map of the "hot spots" that occur in both excitation and emission images, as such areas are often associated with tunneled emission. *In vivo* studies are performed on a human colon adenocarcinoma xenograft tumor model with subcutaneous tumors and a murine breast adenocarcinoma model with aggressive tumor cell metastasis and growth in the lungs. Results demonstrate significant improvements in the reconstructions achieved by the proposed method.
[DOI: 10.1117/1.3149855]

Keywords: fluorescent molecular tomography (FMT); molecular imaging; diffuse optical imaging; turbid media.

Paper 08358RR received Oct. 7, 2008; revised manuscript received Mar. 26, 2009; accepted for publication Apr. 2, 2009; published online Jun. 9, 2009.

1 Introduction

Fluorescence molecular tomography (FMT) is a noninvasive optical functional imaging technique that is emerging as an increasingly important tool in preclinical research and drug development, as it is capable of three-dimensional (3-D) quantification of spatial distribution of molecular agents injected *in vivo*, thus providing a depth-resolved quantitative characterization of specific biological processes occurring several millimeters under the skin.[1,2] Various fluorescent probes have been developed for tagging specific molecular processes.[3] In particular, activated fluorescent probes are designed to activate upon contact with the targeted enzyme or other molecules of interest.[4,5]

In a typical FMT system, the tissue is excited at multiple source locations on the skin using a modulated or continuous-wave (CW) laser source with a wavelength in the near-infrared bandwidth (700 to 900 nm), where tissue has the least absorption.[6] The light emitted by the excited fluorophores is measured on the skin at multiple detector locations and used to reconstruct the spatial distribution of fluorophores in the volume of tissue. The reconstruction problem is highly ill-conditioned, with the system matrix given in terms of the tissue and the measurement geometries and the optical properties of tissue at both excitation and emission wavelengths.[7]

The forward problem underlying FMT concerns the propagation of the excitation photons in tissue based on the diffusion approximation (DA) given the tissue optical properties—namely, absorption and scattering—which are often assumed to be homogenous throughout the tissue volume with values equal to their bulk averages.[1,8] Biological tissue, however, is highly heterogeneous, on both microscopic and macroscopic levels. In particular, macroscopic-level differences in optical absorption can give rise to substantial artifacts in image reconstruction. For example, the heart region is significantly more absorbent than the skin or subcutaneous fat. As a result, light traveling through tissue tends to tunnel into regions of lower relative absorbance. This is demonstrated in Fig. 1, where an excitation image, Fig. 1(a), and the corresponding emission image, Fig. 1(b), of a mouse model with breast tumor injected intravenously with ProSense (VisEn Medical, Bedford, Massachusetts), a protease-activatable near-infrared probe, are obtained in transillumination geometry on the FMT

Address all correspondence to Pouyan Mohajerani, Georgia Institute of Technology, 777 Atlantic Drive NW, Atlanta, GA 30332. Tel: 404-894-4641; Fax: 404-894-4641; E-mail: pouyan@ece.gatech.edu

1083-3668/2009/14(3)/034021/7/$25.00 © 2009 SPIE

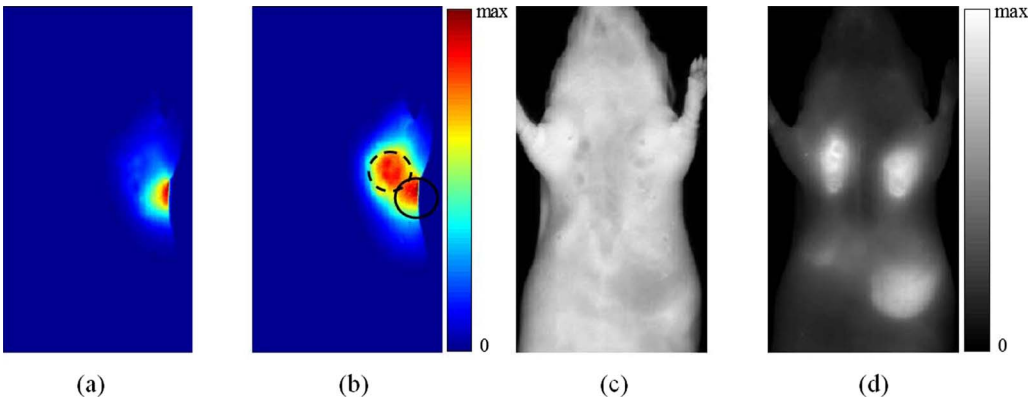

Fig. 1 (a) An excitation image and (b) the corresponding emission image of a mouse model acquired in transillumination geometry. The strong tunneled emission light in the skin flap shown by the solid circle in (b) interferes with the desirable fluorescence from the breast tumor shown by the dashed circle. The front-illumination images obtained in reflectance geometry for the excitation and emission wavelengths are shown in (c) and (d), respectively.

2500 system (VisEn Medical). The front-illumination images for the excitation and emission wavelengths, acquired in reflectance geometry, are shown in Fig. 1(c) and Fig. 1(d), respectively. The high-intensity spots in Fig. 1(d) occurring in the mammary areas are expected, as there is a high concentration of activated probes in these areas. The other bright spot in the lower-right portion of Fig. 1(d) is attributed to the liver, where the probe is metabolized. The light emitted by the fluorophores preferentially tunnels through the skins flaps, shown by the solid circle in Fig. 1(b). The portion of light that reaches the tissue surface due to propagation through low-absorption volumes can have considerably higher intensity than the portion that propagates through the rest of the tissue. This high-intensity portion of light is referred to as "tunneled light" in this paper. We furthermore refer to the strong propagation of light through low-absorption regions of tissue as "tunneling."

This tunneled light adversely affects the reconstruction, as it is comparable to the target emission emanating from the breast tumor, shown by the dashed circle. Note that the strong emission light observed inside the solid circle cannot be attributed to a high concentration of the administered probes inside that region, as is also evident from the front-illumination emission image, Fig. 1(d).

The strong presence of the tunneled light in the emission images can significantly degrade the reconstruction in the targeted regions and also give rise to erroneous or inaccurate attribution of fluorescence concentration to tissue regions prone to significant tunneling, such as skin folds or regions of very thin tissue. Thus, there is a need for a method to detect regions of emission light tunneling in tissue, estimate the component of fluorescence from these regions that is attributable to tunneling effects from neighboring tissue, and subtract this component from the acquired emission images prior to tomographic reconstruction in order to yield a more accurate quantification and allocation of fluorescent agent concentration in the targeted regions.

In this paper, we present a new method for reduction of such artifacts induced by the optical heterogeneities of tissue, especially in absorption, using proper identification of emission image regions that evidence tunneling of the emission light, and compensation of emission images for such tunneling. The method preserves the depth localization accuracy of FMT and improves reconstruction in the targeted areas while eliminating spurious components of fluorescence from the acquired dataset. The proposed method consists of two main steps. In the first step, an estimation of the emission image is obtained from the corresponding excitation image using a linear prediction approach. The resultant residual image is composed mainly of components associated with the targeted fluorescent inclusions. In the second step, a coincidence mask is applied to the residual image for further elimination of the spurious components. The coincidence mask is constructed for each image pair and is a spatial map of the areas where "hot spots" occur in both images; characteristic of tunneled components in the emission image.

The proposed method has been verified using various phantom and animal studies. Here, we provide results from two *in vivo* oncology studies with protease-activatable fluorescent contrast agents: a human colon adenocarcinoma xenograft tumor model with subcutaneous tumors to highlight the benefits of this approach in situations of superficial fluorescent lesions, and a murine breast adenocarcinoma model with aggressive tumor cell metastasis and growth in the lung to demonstrate the benefits of this approach in situations where fluorescence emanates from deeper tissue with starkly different optical properties.

The proposed method is presented in Sec. 2. The *in vivo* results using the proposed method for compensation of the tunneled light are presented in Sec. 3. In Sec. 4 a discussion regarding the performance of the proposed method is presented. Final conclusions are made in Sec. 5.

2 Proposed Method for Compensation of Heterogeneity-Induced Artifacts

The method discussed here uses sets of excitation and emission wavelength transillumination images acquired for multiple source-detector projections to derive estimates of the undesirable contribution of light tunneling to genuine fluorescence. The proposed method is developed based on the observation that light in biological tissue at near-infrared ex-

citation and fluorescence wavelengths separated by a Stokes shift in the range of 20 to 30 nm follows strongly correlated patterns of propagation. Statistical investigations, presented in Sec. 4, have been conducted using multiple pairs of excitation and emission images to analyze the level of correlation between the two images for different *in vivo* models and source locations. Areas of emission light tunneling are accordingly identified based on the strong spatial cross-correlation between the excitation and emission images in regions with significant tunneling.

The proposed method accomplishes this task using a two-step approach. In the first step, components of the emission image that are to a high degree uncorrelated with the excitation image are estimated using a mean square error (MSE) approach. Second, the resultant corrected residual image, composed of fluorescent components uncorrelated with the excitation image, is further corrected using a coincidence mask, intended to mask out the tunneled components remaining in the residual image.

Specifically, let $\mathbf{X}_i$ and $\mathbf{Y}_i$, $i=1\ldots N$, be matrices denoting, respectively, the excitation and the raw emission images obtained at the i'th source for N source positions. The residual image, $\mathbf{R}_i$, is given by

$$\mathbf{R}_i = \mathbf{Y}_i - \mathbf{W}_i * \mathbf{X}_i, \tag{1}$$

where the star ($*$) denotes the convolution operator, and the matrix $\mathbf{W}_i$ is an $L\times L$ linear MSE estimation filter,[9] defined as

$$\mathbf{W}_i = \arg\min_{\mathbf{W}} \|\mathbf{Y}_i - \mathbf{W} * \mathbf{X}_i\|, \tag{2}$$

and given by

$$\mathbf{W}_i = \{\mathbf{A}_{\mathbf{X}}^{-1} C_{(\mathbf{X},\mathbf{Y})}\}, \tag{3}$$

where $\mathbf{A}_{\mathbf{X}}$ and $C_{(\mathbf{X},\mathbf{Y})}$ are the $L^2\times L^2$ autocorrelation matrix for $\mathbf{X}_i$ and $L^2\times 1$ covariance matrix between $\mathbf{X}_i$ and $\mathbf{Y}_i$, respectively, and the operator $\{.\}$ reshapes the $L^2\times 1$ vector operand into an $L\times L$ matrix. The residual image between this optimal estimate and the original emission image thus yields an image of corrected fluorescence.

In Fig. 2, an example of a residual image, Fig. 2(c), is shown for a pair of excitation and emission images, depicted in Figs. 2(a) and 2(b), respectively. These images were acquired for a 4T-1 breast cancer model injected with the cathepsin-activatable agent ProSense on the FMT 2500 tomographic system (VisEn Medical, Bedford, Massachusetts). As seen, the intended fluorescence in the breast is much more noticeable in the residual image than in the raw emission image.

The residual image $\mathbf{R}_i$ is further refined using a coincidence mask identifying regions attributed to the tunneling effect. This operation is necessary as the residual image usually contains small patches of nonnegligible pixels left in areas where tunneling is dominant, as observed in Fig. 2(c) in the upper-left corner close to the boundary of the animal. This is due to the limited estimation capability of the optimal filter for a given estimator size, L (see Sec. 4). The coincidence mask is intended to suppress the components in the residual image that fall within areas with strong indication of tunneling and is derived for each image pair as follows. First, an

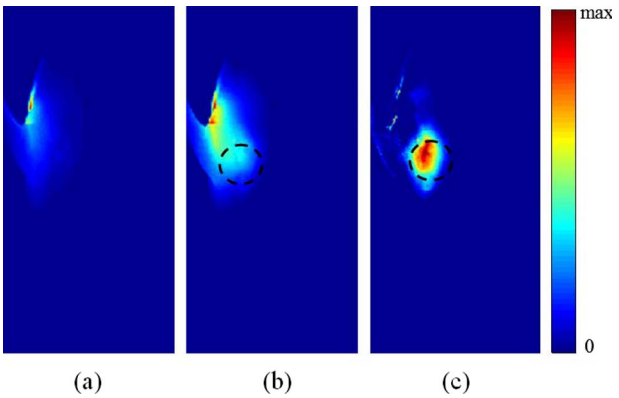

Fig. 2 (a) An excitation image, (b) the corresponding raw emission image, and (c) the residual image obtained from optimal estimation of the emission image from the excitation image. As seen, the desirable tumor signal, denoted by the dashed circles, is significantly better distinguished in the residual image (mouse orientation same as in Fig. 1).

"image mask" is constructed for each image representing the areas in the image that show a relatively strong signal in a relatively small area. In other words, an image mask represents the hot spots in a given image and is constructed for each image to consist of pixels with a magnitude larger than a multiple of the local average. This image mask is further refined using morphological dilation to cover small holes. The coincidence mask is then found as the logical AND of the image masks derived for the excitation and emission images. This is justified, as the tunneled areas tend to form hot spots that appear in both images.

Specifically, for an image $\mathbf{I}$, the corresponding image mask $\mathbf{I}_m$ is a binary matrix of the same dimensions and is given by

$$\mathbf{I}_m = \Im(\mathbf{I} > \alpha \mathbf{F} * \mathbf{I}), \tag{4}$$

where $\Im(\cdot)$ is a morphological dilation operator[10] acting on the binary matrix operand, and α is an empirically determined threshold. The coincidence mask for image pair $(\mathbf{X},\mathbf{Y})$ is then a binary matrix of the same dimensions given by

$$\mathbf{M}_{(\mathbf{X},\mathbf{Y})} = \mathbf{X}_m \wedge \mathbf{Y}_m, \tag{5}$$

where $\wedge$ denotes the logical AND operation. The final corrected emission image is then given by

$$\mathbf{Y}_i^c = \mathbf{R}_i \otimes (1 - \mathbf{M}_{(\mathbf{X}_i,\mathbf{Y}_i)}), \tag{6}$$

where $\mathbf{R}_i$ is the residual given in Eq. (1), and $\otimes$ represents the element-by-element matrix multiplication.

Figure 3 depicts a raw emission image and the final result of the correction as achieved by the proposed method. The images were acquired from a 4T-1 model injected with ProSense with the same mouse body orientation as in Fig. 1. The images in Fig. 1 and Fig. 3 are obtained for different experimental conditions and mice. As seen, the desirable emission signal coming from the breast tumor, enclosed in dashed ellipses, is properly distinguished in the corrected image as opposed to the raw image, where the tumor signal is strongly shadowed by the tunneled light.

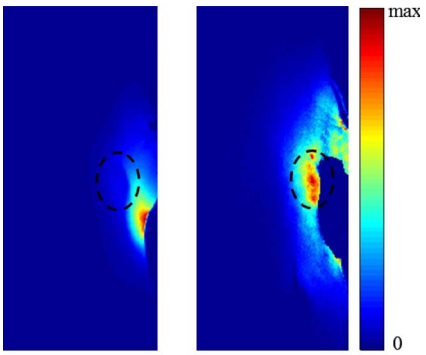

Fig. 3 (a) A raw emission image and (b) the result of tunneling correction using the proposed method (mouse body orientation same as in Fig. 1). The fluorescence emanating from the tumor, denoted by the dashed ellipses, is much better distinguished in (b).

The resulting final emission images, $\mathbf{Y}_i^c$, and the corresponding excitation images are then used to form the normalized Born ratio[11] prior to proceeding with FMT reconstruction as described elsewhere.[1]

3 *In Vivo* Validation and Results

We have applied the proposed method to several phantom and *in vivo* tomographic imaging situations with a broad range of fluorescence depths, imaging agents, and anatomical locations. Here, we highlight two particular *in vivo* models spanning subcutaneous to deeper tissue regions, in solid tumors and air-filled lungs, respectively.

Cathepsin B, a lysosomal cysteine protease present in normal cells and tissues, has been shown to increase in premalignant and malignant tumors.[12,13] In the first model, 3×10^6 HT-29 human colon adenocarcinoma cells were injected subcutaneously in the mammary fat pads of Nu/Nu mice, leading to detectable tumor masses within one week. ProSense was injected intravenously to highlight the cathepsin activity associated with tumors, and this fluorescence was quantified 24 h postinjection using the FMT 2500 system (VisEn Medical, Bedford, Massachusetts). Figure 4(a) illustrates a volume rendering from the FMT reconstruction showing apparent activation of the agent from a broad, diffuse region covering the chest and upper abdomen of the animal. Figure 4(b), gated identically to the previous image, very clearly highlights the sites of tumor activation of the agent, having taken into account the emission light tunneling according to the method presented in Sec. 2.

4T-1 murine breast adenocarcinoma cells also produce cathepsin B,[14] among other proteases capable of cleaving ProSense. BALB/c mice were injected intravenously with 5×10^5 4T-1 murine breast adenocarcinoma cells, thus leading to aggressive tumor cell metastasis and growth in the lung within two weeks. ProSense was injected intravenously to highlight the protease activity associated with lung metastasis, and this fluorescence was also quantified 24 h postinjection using FMT. The quantitation of ProSense fluorescence corresponded to the tumor burden as assessed by both visual examination and histological analysis of the lungs (data not shown). Figures 5(a) and 5(b) again illustrate the improvement in 3-D spatial allocation of fluorescent contrast agent concentration in the lung cavity corresponding to the metastatic nodules. In this case, the fluorescence emanates from deeper tissue than the previous model—namely, from near the center of the lung cavity.

This comparison between the two models confirms the broad benefits of this method for *in vivo* imaging but also serves to highlight the robustness of the tunneling compensation technique across tissue regions with markedly different absorption and scattering coefficients.

4 Discussion

The main contribution of this paper is to demonstrate a new technique for the reduction of the artifacts in fluorescence molecular tomography (FMT) caused by the strong light propagation through low-absorption tissues in small animal studies. These artifacts result in considerable error in the reconstructed FMT image. Our technique is based on a simple

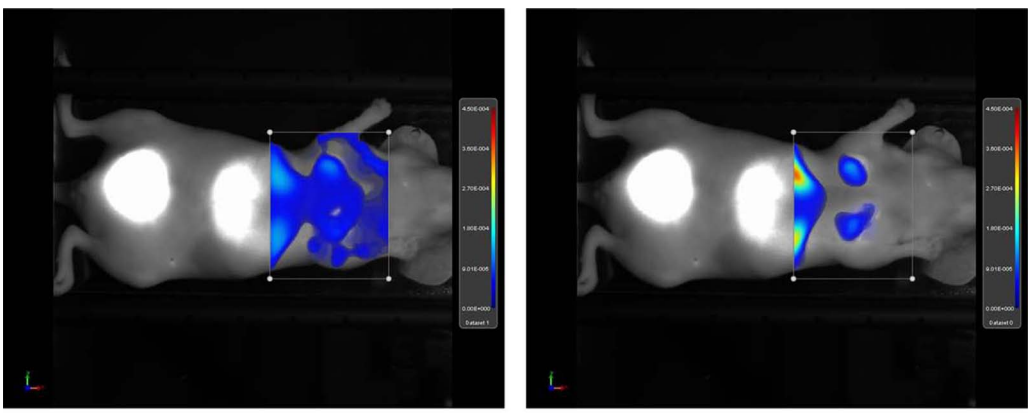

Fig. 4 Illustrative results displaying 3-D volume renderings from FMT tomographic reconstruction of an HT-29 human colorectal adenocarcinoma xenograft model (a) without tunneling compensation and (b) with tunneling compensation. Color-coded contours indicate agent concentration, with identical gating in both images. The grayscale front-illumination emission images are shown for reference. (Color online only.)

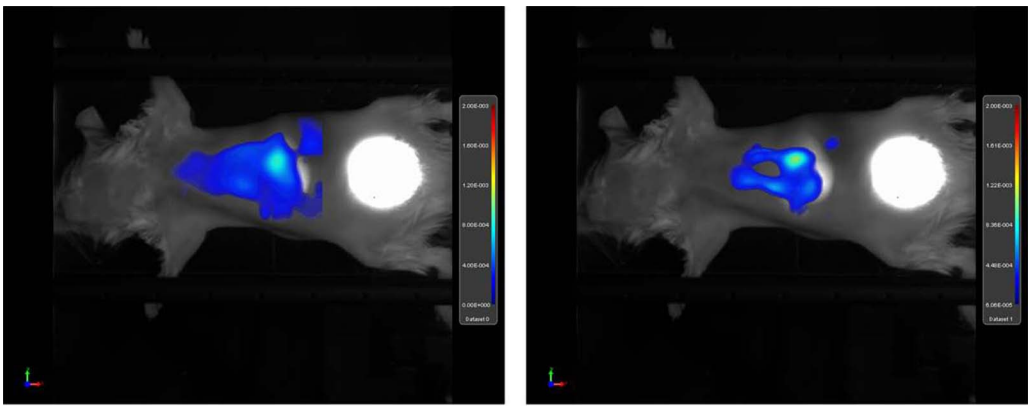

(a) (b)

Fig. 5 Illustrative results displaying 3-D volume renderings from FMT tomographic reconstruction of a 4T-1 murine breast adenocarcinoma with lung metastasis (a) without tunneling compensation and (b) with tunneling compensation. Color-coded contours indicate agent concentration, with identical gating in both images. The grayscale front-illumination emission images are shown for reference. (Color online only.)

preprocessing of the imaging data to considerably reduce the effect of contributions that reach the detector by propagating mainly through the low-absorption tissue. To implement this technique, we use a preprocessing step "prior" to the application of the forward model and inversion. This preprocessing step is based on the spatial correlation between excitation and fluorescence raw images and the consequent generation of a filter applied to the raw images. To model the tissue in our method, we assume uniform optical properties (by using average values for μ_a and μ_s). It should be mentioned that a properly implemented higher order forward model is a more systematic way to solve such problems, and it will result in more accurate image reconstructions compared to our technique. However, such higher-order models become relevant only if we have a reasonably accurate model for the spatial distribution of the optical properties of the animal tissue. Unfortunately, obtaining such detailed information that can be applied to all animals under study is not practical for the *in vivo* scenarios studied in this paper. It can be envisioned that methods combining multiple modalities could be developed to gather such information, but this is beyond the scope of this work.

In this section, we analyze and discuss the correlation between excitation and emission images, the trade-offs involved in adjusting the parameters of the proposed algorithm, and the computational complexity of the proposed method. Furthermore, we present a case study demonstrating the capability of the proposed method in distinguishing tunneled fluorescence and desirable fluorescence emanating from within thin and low-absorption tissue using a *post mortem* flank implant.

The strong correlation between the excitation and emission images was used in the development of the tunneling compensation algorithm presented in Sec. 2. Here, we present a statistical study of the level of such correlation using a set of image pairs acquired from two *in vivo* models. To assess the level of the correlation between the two images, we evaluate the components of the emission image that are predictable from the corresponding excitation image. Specifically, a given emission image is projected into the space spanned by the corresponding excitation image and its spatially shifted copies. This is equivalent to linearly predicting the emission image from the excitation image using an optimal two-dimensional (2-D) filter, as was performed in Sec. 2 in the construction of the residual signal. It is observed that a significant portion of the emission image is predictable from, and therefore correlated with, the corresponding excitation image. Such a statistical analysis is presented in Fig. 6. The x axis in Fig. 6 denotes the lateral length, L, of the square filter used for linear prediction of the emission image from the excitation image in dimensionless units—i.e., normalized to the maximum filter length employed in the statistical analysis. The y axis is the percentage of the emission signal energy that is

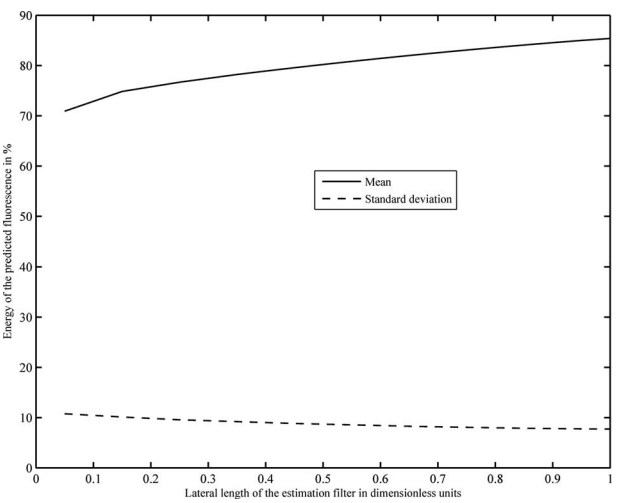

Fig. 6 The mean (solid line) and the standard deviation (dashed line) of the energy of the predicted emission signal, obtained after optimal estimation of the emission image from the excitation image, relative to the energy of the raw emission signal, expressed in percentage [see Eq. (7)]. The x axis denotes the lateral length of the square 2-D optimal estimator, normalized to the maximum filter length employed. The statistics have been obtained over 98 image pairs acquired from two *in vivo* cases. The relatively high average energy of the predicted signal and its low variance over the dataset suggest a high level of correlation between the excitation and emission images.

predictable from the excitation signal and is given by

$$E = 100 \times (1 - \|\mathbf{R}\|/\|\mathbf{Y}\|), \quad (7)$$

where **Y** and **R** are the emission and the corresponding residual image, respectively [see Eq. (2)]. A 100% value for E, therefore, implies perfect prediction. The statistics depicted in Fig. 6 are obtained over a database of 98 image pairs for a 4T-1 model injected with ProSense and a 4T-1 model injected with a matrix metalloproteinase activatable agent, MMPSense (VisEn Medical, Bedford, Massachusetts).

It should be noted that this high level of correlation between the excitation and emission images is not due to the bleed-through signal—i.e., the fraction of the excitation light that passes through the emission filter. The bleed-through signal has an average energy of only 3×10^{-5} of the emission signal energy, as calculated by taking into account the bandpass emission filter's rejection at the excitation wavelength and the exposure times and source powers used during acquisition of the image pairs. The bleed-through signal is conventionally subtracted from the emission signal prior to Born normalization.[15] We found this subtraction to be unnecessary after the tunneling compensation is applied to the emission images, as the tunneling compensation subtracts a much larger fraction of the excitation image from the emission image in calculating the residual image.

The main trade-off involved in parameter adjustment is between contrast and accuracy. Eliminating many components from the emission image, while likely to increase the contrast, might result in erroneous reconstructions and loss of depth resolution. The parameters involved in the proposed method include the estimation filter lateral length L and the parameters in the coincidence mask generation algorithm—namely, the filter **F** and the multiplier factor α [see Eq. (4)]. Generally, a larger value for L results in subtraction of a larger portion from the emission image. Also, a smoother filter **F** and a smaller value of α result in a less relaxed, more restrictive mask—namely, one with larger patches with values of one. The parameters are adjusted based on many measurement sets obtained from resin phantoms and *in vivo* models. For instance, fluorescent tubes inserted at different depths in a resin phantom were imaged and the parameters were adjusted so as to retain the correct depth in the reconstructions while still correcting for the tunneling in the *in vivo* cases.

The computational complexity of the proposed method is negligible compared to the overall complexity of the reconstruction algorithm. The most numerically expensive step of the tunneling compensation algorithm is the computation of the optimal estimation filters, as it involves several matrix multiplications for calculation of the autocorrelation matrices and covariance vectors [see Eq. (3)]. The coincidence mask generation involves only simple 2-D filtering using preset filters and logical operations on pixels.

It should be further noted that, while most of the spurious components of the emission image emanate from thin or low-absorption tissue, the proposed method does not distort the desirable emission signal coming from targeted lesions located in or around such tissue volumes. This is illustrated in Fig. 7, where a tube filled with a fluorescent solution is implanted in the flank of the mouse *postmortem* and imaged without, Fig. 7(a), and with, Fig. 7(b), the tunneling compensation. The position of the implanted tube can be roughly seen in the front-illumination reflectance emission image, Fig. 7(c). As seen, the tube is properly retained in the compensated reconstructed image, Fig. 7(b).

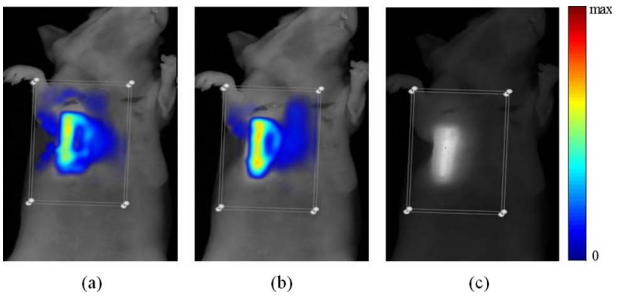

Fig. 7 The proposed tunneling compensation method applied to a *postmortem* flank implant model. The results of reconstruction using raw data and post-processed data are shown in (a) and (b), respectively. As seen, the proposed method properly retains desirable emission signal emitted from within thin and low-absorption flank tissue. The corresponding front-illumination emission image is shown in (c) for reference. The white box depicts the volume inside which the fluorophore distribution is reconstructed.

Last, the method proposed here is essentially about improving the target-to-background ratio. The selection of what constitutes target (tumor in this case) and what constitutes background (any tissue region with no agent uptake) is a subjective matter, being based on biological interpretation of disease progression and protease expression in different tissues. To resolve this objectively, one would have to subject homogenates of tissue samples from the entire animal to immunoblot- or immunostaining-type analyses (such as Western blots or enzyme-linked immunosorbant assays, respectively) to detect specific proteins and then compare those against enzymatic panels of what activates the agent in question. Here, we have relied on knowledge of the disease model and contrast agent pairing to determine that the areas of specific uptake are confined to the tumors and that the flanks of the animal and other areas of the thorax are agent-free, both observations being confirmed by the image reconstruction improvements introduced in this paper.

5 Conclusion

A method was presented here for identification, estimation, and correction of the spurious components that arise in the emission images due to tunneling of emission light through thin tissue or volumes of low absorption typical of fatty tissue and skin flaps. The proposed method utilizes the significant correlation between excitation and emission images to estimate the desirable components (as opposed to the tunneled components) of the emission image using optimal MSE estimation of the emission image from the excitation image. A coincidence mask was further proposed and applied to suppress the image components highly attributable to tunneling. Two *in vivo* studies were presented to illustrate the efficacy of the proposed method in improving the accuracy of the tomographic reconstruction algorithms.

References

1. R. B. Schulz, J. Ripoll, and V. Ntziachristos, "Experimental fluorescence tomography of tissues with noncontact measurements," *IEEE Trans. Med. Imaging* **23**(4), 492–500 (2004).
2. V. Ntziachristos, "Fluorescence molecular imaging," *Annu. Rev. Biomed. Eng.* **8**, 1–33 (2006).
3. K. Licha, "Contrast agents for optical imaging," *Top. Curr. Chem.* **222**, 1–29 (2002).
4. R. Weissleder, C.-H. Tung, U. Mahmood, and A. Bogdanov Jr., "*In vivo* imaging of tumors with protease-activated near-infrared fluorescent probes," *Nat. Biotechnol.* **17**(4), 375–378 (1999).
5. E. Chang, J. Sun, J. S. Miller, W. W. Yu, V. L. Colvin, J. L. West, and R. Drezek, "Protease-activated quantum dot probes," *Proc. SPIE* **6191**, 61911E.1–10 (2006).
6. A. P. Gibson, J. C. Hebden, and S. R. Arridge, "Recent advances in diffuse optical imaging," *Phys. Med. Biol.* **50**(4), 1–43 (2005).
7. A. Cong and G. Wang, "A finite-element-based reconstruction method for 3-D fluorescence tomography," *Opt. Express* **13**(24), 9847–9857 (2005).
8. H. Jiang, "Frequency-domain fluorescent diffusion tomography: a finite-element-based algorithm and simulations," *Appl. Opt.* **37**(22), 5337–5343 (1998).
9. M. H. Hayes, *Statistical Digital Signal Processing and Modeling*, Wiley, New York (1996).
10. J. Serra, *Image Analysis and Mathematical Morphology*, Academic Press, New York (1983).
11. A. Soubret, J. Ripoll, and V. Ntziachristos, "Accuracy of fluorescent tomography in the presence of heterogeneities: study of the normalized Born ratio," *IEEE Trans. Med. Imaging* **24**(10), 1377–1386 (2005).
12. T. K. S. Krueger, H. Wolf, U. Kellner, and A. Roessner, "Interactions between human colon carcinoma cells, fibroblasts and monocytic cells in coculture—regulation of cathepsin B expression and invasiveness," *Cancer Lett.* **223**(2), 313–322 (2005).
13. M. D. D. De Stefanis, A. Dragonetti, J. J. Houri, E. Ogier-Denis, P. Codogno, F. M. Baccino, and C. Isidoro, "Differentiation-induced changes in the content, secretion, and subcellular distribution of lysosomal cathepsins in the human colon cancer HT-29 cell line," *Cell Tissue Res.* **289**(1), 109–117 (1997).
14. D. C. B. Parker, B. Bidwell, F. Gago, M. Fanelli, J. George, J. Slavin, A. Möller, R. Steel, N. Pouliot, B. Eckhardt, M. Henderson, and R. Anderson, "Primary tumor expression of the cysteine cathepsin inhibitor Stefin A inhibits distant metastasis in breast cancer," *J. Pathol.* **214**(3), 337–346 (2008).
15. V. Ntziachristos and R. Weissleder, "Experimental three-dimensional fluorescence reconstruction of diffuse media by use of a normalized Born approximation," *Opt. Lett.* **26**(12), 893–895 (2001).